Calibration of Six Constitutive Material Models for Geomaterial

Hamid Rokhy[1], Reza Nasouri[2], Arturo Montaya[2], Adolfo Matamoros[2], Roya Bakzadeh[3]

[1]Department of Aerospace Engineering, Amir Kabir University of Technology, Tehran, Iran
[2]Department of Civil and Environmental Engineering, University of Texas at San Antonio, TX, U.S
[3]Department of Mining Engineering, Urmia University, Iran

Abstract

Recently, several constitutive material models have been developed and added to the LS-DYNA library to predict concrete geomaterial behavior. These developments were established merely from using concrete compressive strength, which limits the level of robustness in capturing actual concrete behavior. This study focuses on developing a simplified approach to calibrate six constitutive material models including Soil and Foam, Pseudo Tensor, Geological Cap Model, Concrete Damage Model Rel-3, Johnson Holmquist, and Continues Surface Cap Model against Triaxial and Hydrostatic Compression Tests (TXC and HCT) data. Comparisons between individual numerical results were performed to evaluate whether accuracy can be offered through a corresponding constitutive material model. The presented calibration method can also be applied to different geomaterials such as rock and soil.

1 Introduction

Geomaterials (soil, concrete and rock) behave very differently from metals. For metals, the stress-strain curve can be easily obtained using the tensile test, while geomaterials will need to be subjected to other testes because of their completely different behavior. The difference in the behavior of geomaterials from metals can be summarized as follows:

1. Geomaterials tensile strengths are small compared to their compressive strengths.

2. Geomaterials are relatively compressible (i.e., pressure-volume response). As shown in Figure.1, for a typical geomaterial, pressure versus volume strain (compaction) response can be divided into three phases:

2.1 $P_0 < P < P_1$: the initial elastic response. The elastic bulk modulus (K) is the slope of this segment.

2.2 $P_1 < P < P_2$: when the pores (voids) in the materials are compressed.

2.3 $P_2 < P$: voids removal results in a fully compacted material.

3. As with metals, it is the shear stress that is typically used to characterize a material strength through the use of a constitutive model. However, the shear strength of geomaterials increases with increasing mean stress (confinement), as shown in Figure 1.

4. In the case of impact and blast loading due to high strain rate, the strength of geomaterials exhibite non-linear increase which should not be neglected.

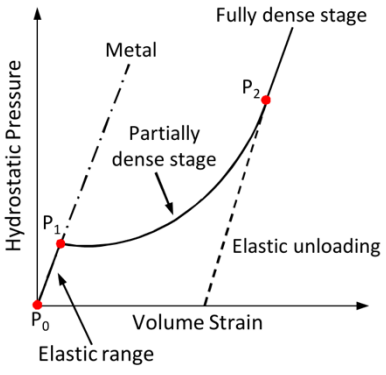

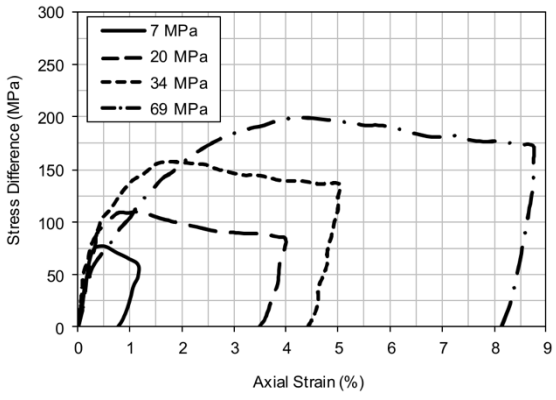

Fig.1: Left: Schematic of pressure versus volume response for a geomaterial, Right: The dependency of the shear strength of geomaterials to mean stress

The constitutive material models used to replicate geomaterials behavior must be able to properly capture all the four phases described above. Some of the available material models such as Soil and Foam (MAT_005), Pseudo Tensor (MAT_016) and Geologic Cap Model (MAT_025) can only predict a few phases, while other liberies like Concrete Damage Rel-3 (MAT_072R3) or CSCM (MAT_159) can precisely predict these behaviors if properly calibrated.

To determine geomaterials behavior, data of three laboratory tests, i.e., Unconfined Compression Test (UCT), Hydrostatic Compression Test (HCT), and Triaxial Compression Test (TXC) are implemented.

In the Unconfined Compression Test, the geomaterial specimen was subjected to axial loading reach to failure point. Here, the compressive stress at which the specimen failed is considered as the compressive strength of the geomaterial. In the Hydrostatic Compression Test, the specimen is subjected to the same axial and lateral loads and volumetric strains are recorded. Finally, hydrostatic pressure change with respect to volumetric strains will be obtained.

In the Triaxial Compression Test, axial and lateral loads do not remain the same. In this way, the specimen is first subjected to the same axial and lateral loading until certain pressure is reached. After that, by keeping the lateral load constant, the axial load will continue until the specimen reaches the failure point. Finally, the increase in specimen strength is determined for several different confinement pressures. The schematic of these experimental tests is shown in Figure 2.

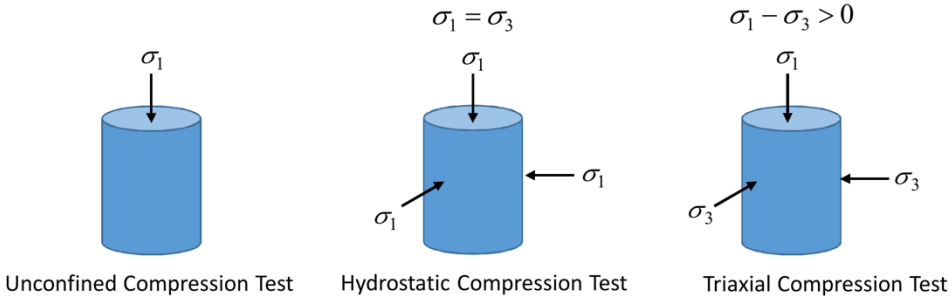

Fig.2: Typical geomaterial cylindrical specimen under UCT, HCT and TXC

2 Calibration of Soil Material Models

To investigate the accuracy of the soil constitutive material models available in LS-DYNA, each model was calibrated using the TXC and HCT test data followed by comparing the numerical results against the experiments. Density, module of elasticity and poisson's ratio of the employed sand were 1830 Kg/m^3, 80 MPa and 0.35, respectively [1]. Bulk modulus (k) and the shear modulus (K) were determined to be 88.89 MPa and 29.63 MPa, respectively. The TXC and HCT test data are shown in Figure 3.

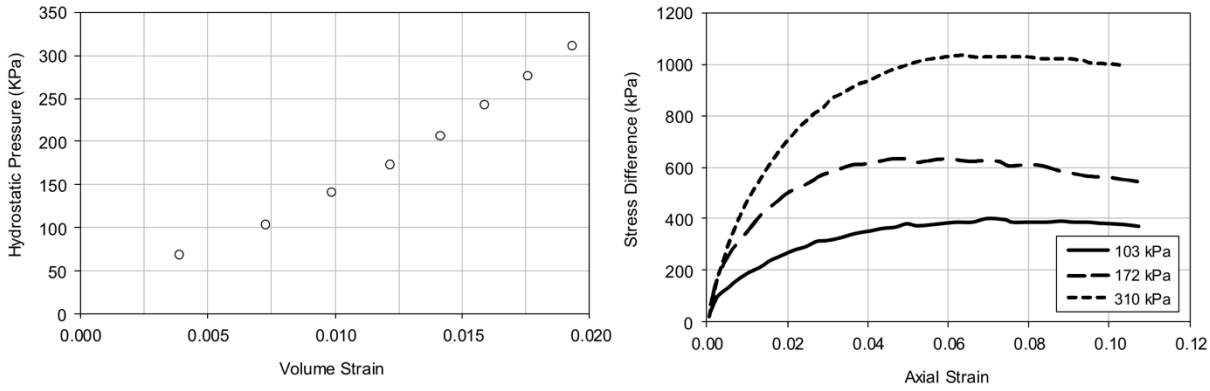

Fig.3: Experimental results for HCT (left) and TXC at different confining pressures (right) of unsaturated Bank sand [1]

2.1 MAT_005 (Soil and Foam)

MAT_005 material model requires a minimum amount of input data, thus it has been frequently used to simulate the behavior of geomaterials such as soil, and concrete. In this model, the material is considered to be elastoplastic and pressure dependant. As described by Drucker–Prager yield criterion, the deviatoric perfectly plastic yield function (ϕ) is defined in terms of the second stress invariant J_2, hydrostatic pressure (p) and three constant values of a_0, a_1 and a_2 as shown in Eq. (1).

$$\phi = J_2 - \left(a_0 + a_1 p + a_2 p^2\right) \tag{1}$$

In the yield surface, $\sigma_e = \sqrt{3J_2}$, is the effective stress (von Mises stress) which can be re-written as

$$\sigma_e = \left[3\left(a_0 + a_1 p + a_2 p^2\right)\right]^{\frac{1}{2}} \tag{2}$$

In the Triaxial Compression Test (TCT), the effective stress σ_e is equal to the difference between the axial and lateral stress (stress difference), Eq. (2) can be expressed as follows:

$$\sigma_1 - \sigma_3 = \left[3\left(a_0 + a_1 p + a_2 p^2\right)\right]^{\frac{1}{2}} \tag{3}$$

In addition, the shear stress (τ) at failure can be described in terms of the soil cohesion (c) and friction angle (θ) using the Mohr-Coulomb model (Figure.4).

$$\tau = c + p\tan(\theta) \tag{4}$$

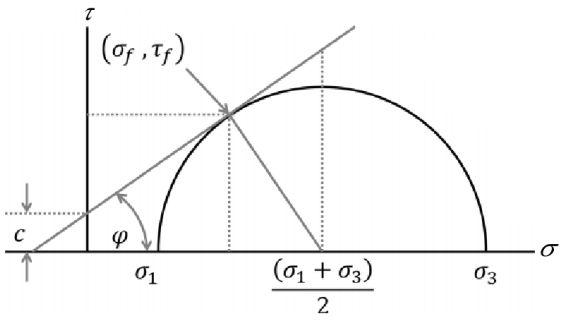

Fig.4: The illustration of Mohr's circle geometry

Employing $\tau = \frac{\sigma_1 - \sigma_3}{2}$ accompanied by Eq. (3) and (4), the constant coefficients a_0, a_1 and a_2 can be obtained using the following equations:

$$a_0 = \frac{4c^2}{3} \tag{5}$$

$$a_1 = \frac{8c\tan(\theta)}{3} \tag{6}$$

$$a_2 = \frac{4\ tan^2(\theta)}{3} \tag{7}$$

Note that the hydrostatic pressure is defined based on the volumetric strain. The volumetric strain is evalueated by the natural log of the relative volume and is negative in compression. Relative volume is a ratio of the current volume to the initial volume at the start of the calculation. The volumetric strain is described in terms of the measured (engineering) volume strain ε_{kk} as presented in Eq. (8).

$$\ln\left(\frac{V}{V_0}\right) = \ln\left(1 - \varepsilon_{kk}\right) \tag{8}$$

To construct the Mohr's circles pertinent to the Bank sand (plotted in Figure 5), the peak stress difference (deviatoric stress) and the corresponding confining pressure were utilized. Tangent to these three Mohr circles was drawn to estimate the Mohr-Coulomb failure envelope. As illustrated, cohesion c and friction angle ϕ were estimated to be 20.1 kPa and 37.3°.

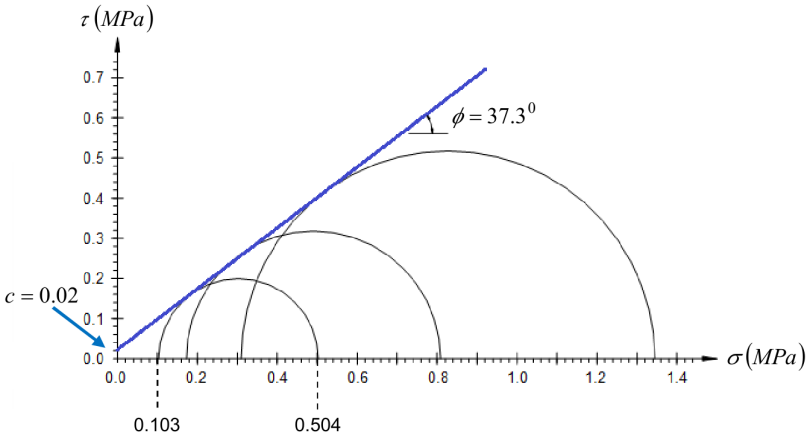

Fig.5: Mohr-Coulomb failure envelope from the Triaxial compression test data

Material parameters calibrated for MAT_005 are summarized in Table 1. Note that the volumetric strain refers to the natural log value of the relative volume calculated using the data in Figure 3 and Eq. (8).

Yield surface		Volumetric strain		Pressure (MPa)	
a_0	5.4E-4	EPS1	0.0	P1	0.0
a_1	0.0408	EPS2	-0.0039	P2	0.0687
a_2	0.7738	EPS3	-0.0073	P3	0.1038
		EPS4	-0.0099	P4	0.1403
		EPS5	-0.0123	P5	0.1724
		EPS6	-0.0143	P6	0.2061
		EPS7	-0.0160	P7	0.2426
		EPS8	-0.0177	P8	0.2762
		EPS9	-0.0195	P9	0.3113

Table 1: Material parameters calibrated through experimental data for MAT_005

2.2 MAT_016 (Pseudo Tensor)

MAT_016 is similar to MAT_SOIL_AND_FOAM, in that the material response to loading is primarily described in terms of a pressure-volume curve and a shear failure surface. Like the MAT_005, the pressure volume envelope is described using a piecewise curve, although MAT_PSEUDO_TENSOR also allows variations in bulk unloading modulus to be specified as a function of volumetric strain. The shear failure surface in the MAT_016 can be defined in one of two ways — in the first, the variation in shear strength with confinement is described as a simple piecewise curve, while the second method uses a pressure dependent shear failure surface as Eq. (9):

$$\sigma_1 - \sigma_3 = a_0 + \frac{p}{a_1 + a_2 p} \tag{9}$$

The constant coefficients a_0, a_1 and a_2 can be obtained using the Mohr-Coulomb model. In the MAT_016, the parameter a_2 defines the non-linearity of the yield surface, so when using direct calculation from Mohr -Coulomb parameters, a_2 should be set to zero. According to Eq. (4) and (9), the constant coefficients a_0 and a_1 can be obtained by using the following equations:

$$a_0 = 2c \tag{10}$$

$$a_1 = \frac{1}{2\tan(\theta)} \tag{11}$$

Strain rate effects in MAT_016 are accounted for by the use of a strain rate multiplier curve, defining the increase in yield strength ($\sigma_1 - \sigma_3$) as a function of strain rate. Given that the yield surface as a whole is scaled while pressure dependency remains constant, this approach allows control over the soil's cohesive response as a function of strain rate.

In this material model similar to the MAT_005 (Soil and Foam), the hydrostatic pressure is defined based on the volumetric strain using Eq. (8). The calculated values are expressed in tabular form (up to 10 point) using the Tabulated Compaction equation of state. Material parameters calibrated for MAT_016 are summarized in Table 2.

Yield surface		Volumetric strain		Pressure (MPa)	
a_0 (MPa)	0.0402	ev1	0.0	c1	0.0
a_1	0.6563	ev2	-0.0039	c2	0.0687
a_2	0.0	ev3	-0.0073	c3	0.1038
		ev4	-0.0099	c4	0.1403
		ev5	-0.0123	c5	0.1724
		ev6	-0.0143	c6	0.2061
		ev7	-0.0160	c7	0.2426
		ev8	-0.0177	c8	0.2762
		ev9	-0.0195	c9	0.3113

Table 2: Material parameters calibrated through experimental data for MAT_016

2.3 MAT_025 (Geologic Cap Model)

MAT_025 is an inviscid two-invariant geologic cap model. In this material model, the yield surface is plotted in the first and second invariants of the stress tensor space $\left(\sqrt{J_2} - I_1\right)$. The first invariant is the trace of the stress tensor and equal to $3p$.

As shown in Figure 6, the Cap model is comprised of the fixed yield surface f_1, the yield cap surface f_2, and the tension cutoff surface f_3 in the $\sqrt{J_2} - I_1$ space. The fixed yield surface f_1 can be considered as a failure surface, where region above the failure surface is not permissible. The fixed yield surface f_1 is described in terms of the first stress invariant I_1 and several constants α, θ, γ and β as Eq. (12).

$$\sqrt{J_2} = f_1(I_1) = \alpha - \gamma\exp(-\beta I_1) + \theta I_1 \tag{12}$$

In the above formula, if $\gamma = \beta = 0$, it can be written in a simpler form below:

$$\sqrt{J_2} = f_1(I_1) = \alpha + \theta I_1 \tag{13}$$

According to Eq. (4), the constant coefficients α and θ can be obtained from Mohr -Coulomb model by using the following equations.

$$\alpha = \frac{6c\cos(\theta)}{\sqrt{3}(3-\sin(\theta))} \tag{14}$$

$$\theta = \frac{2\sin(\theta)}{\sqrt{3}(3-\sin(\theta))} \tag{15}$$

The yield cap surface f_2 is a moving yield surface. The yield cap surface follows the shape of an ellipse and is represented by Eq. (16) in the $\sqrt{J_2} - I_1$ space.

$$f_2 = R^2 J_2 + (I_1 - C)^2 = R^2 b^2 \tag{16}$$

Where R is the shape factor and is the ratio of the major to minor axis of the ellipse, and $R.b = (X - C)$. Note that X is the value of I_1 at the intersection of the yield cap surface and the I_1 axis, C is the value of I_1 at the center of ellipse and b is the value of $\sqrt{J_2}$ when $I_1 = C$.

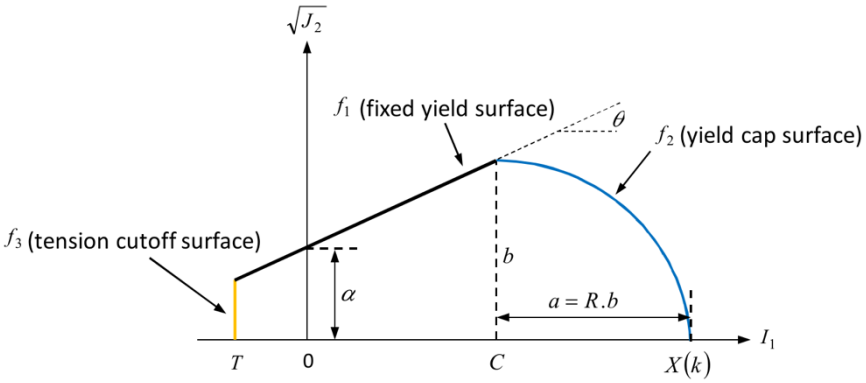

Fig.6: Schematic of cap model ($\gamma = \beta = 0$)

In this model, the hydrostatic pressure is defined based on the plastic volume strain as Eq. (17).

$$\varepsilon_v^p = W\{1 - \exp[-D(X - X_1)]\} \tag{17}$$

Where ε_v^p is the plastic portion of the volume strain, W characterizes the maximum plastic volumetric strain as shown in Figure 7, D is constant parameter, X represents the first invariants of the stress tensor, and X_1 is pressure at which compaction initiates in isotropic compression, i.e. $X - X_1 = 3(P - P_1)$.

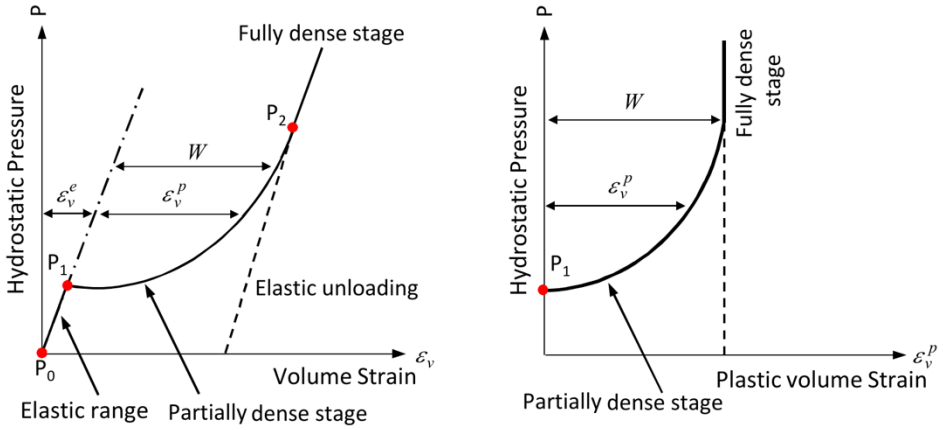

Fig.7: The equation of state for MAT_025

Most soils exhibit plastic deformation even at very low stress level, hence it is reasonable to assume that $X_1 = 0$ is negligibly small for most soils [2]. So, Eq. (17) can be rewritten as:

$$-\ln\left(1 - \frac{\varepsilon_v^p}{W}\right) = D(X) \tag{18}$$

The plastic volume strain ε_v^p is obtained from the following equation.

$$\varepsilon_v^p = \varepsilon_v - \frac{p}{K} \tag{19}$$

Where ε_v is the volume strain and K is bulk modulus.

In the previous section, the cohesion c and friction angle θ were estimated to be 20.1 kPa and 37.3°, respectively. According to the Eqs. (14) and (15), the constant coefficients α and θ are obtained as 0.0231, and 0.292, respectively.

Using the results of hydrostatic compression tests presented in Figure 3, it is possible to estimate the relationship between hydrostatic pressure and plastic volume strain according to Eq. (18). According to hydrostatic compression test data shown in Figure 3, the values of $-\ln\left(1-\varepsilon_v^p/W\right)$ are calculated in terms of X, which are documented in Table 3. Here, the maximum plastic volume strain W is assumed to be 0.03. As shown in Figure 8, the parameter of D (the slope of variations of $-\ln\left(1-\varepsilon_v^p/W\right)$ versus X), is obtained as 0.7929.

ε_v	p (MPa)	ε_v^p	$-\ln\left(1-\varepsilon_v^p/W\right)$	X (MPa)
0.0039	0.0687	0.0031	0.2060	0.1102
0.0073	0.1038	0.0061	0.3113	0.2286
0.0099	0.1403	0.0083	0.4209	0.3234
0.0122	0.1724	0.0102	0.5173	0.4175
0.0142	0.2061	0.0118	0.6182	0.5020
0.0159	0.2426	0.0132	0.7278	0.5774
0.0176	0.2762	0.0145	0.8286	0.6591
0.0193	0.3113	0.0158	0.9338	0.7487

Table 3: Estimation of $-\ln\left(1-\varepsilon_v^p/W\right)$ versus X for MAT_025

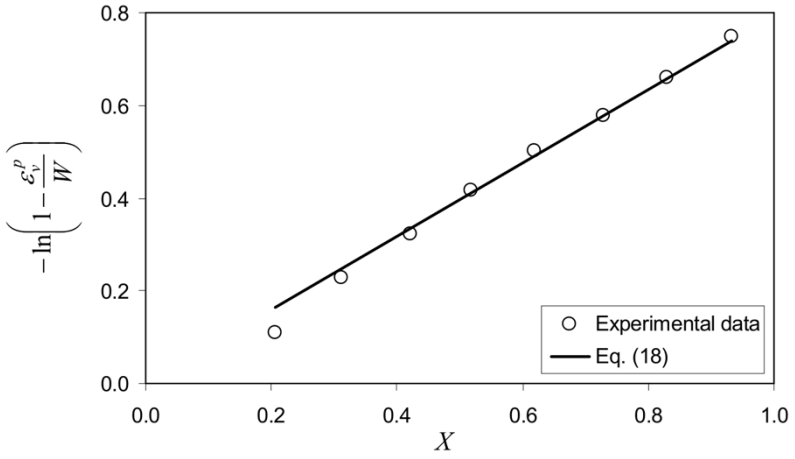

Fig.8: Estimation of the relationship between hydrostatic pressure and plastic volume strain by MAT_025

Material parameters calibrated for MAT_025 are summarized in Table 4. Based on laboratory observations, the value of parameter R could range from 1.67 to 2.0 for most soils [3]. To determine the value of R, it is required to know the approximate size and shape of the yield cap surface f_2. However, the value of R was arbitrary assumed to be 3.0 as this value gives reasonable prediction on the stress-strain behavior of the Bank sand.

Yield surface		Plastic volume strain	
α (MPa)	0.0231	R	3.0
θ (MPa)	0.292	D (MPa^{-1})	0.7929
γ (MPa)	0.0	W	0.03
β (MPa)	0.0	X_0 (MPa)	0.0

Table 4: Material parameters calibrated through experimental data for MAT_025

2.4 Numerical validation of constitutive material models

The numerical model was conducted in a single element of 100mm×100mm×100mm with the specified boundary conditions as shown in Figure 9. Two loading conditions are analyzed. These are the triaxial compression test at different confining pressures, and hydrostatic compression test. Before each triaxial test, the single element is subjected to isotropic load until it reaches the desired confining pressure using the keyword “LOAD SEGMENT”. Subsequently, for each confining pressure, the single element is loaded axially in compression using the keyword “BOUNDARY PRESCRIBED MOTION”, while, for the hydrostatic test, only isotropic load is applied to the top and sides surfaces of the element.

Comparisons of the numerical results with TXC and HCT test data reported by Li et al. [1] for different constitutive material models are shown in Figures 10 and 11, respectively. As can be seen, due to the present of yield cap surface in the MAT_025, this model was able to predict TXC significantly better than MAT_005. But since this material model uses a mathematical formula (Eq. (18)) to express the relation between the hydrostatic pressure and the plastic volume strain, it will be less accurate than MAT_005. Also, no difference was observed between MAT_005 and MAT_016 for Bank soil.

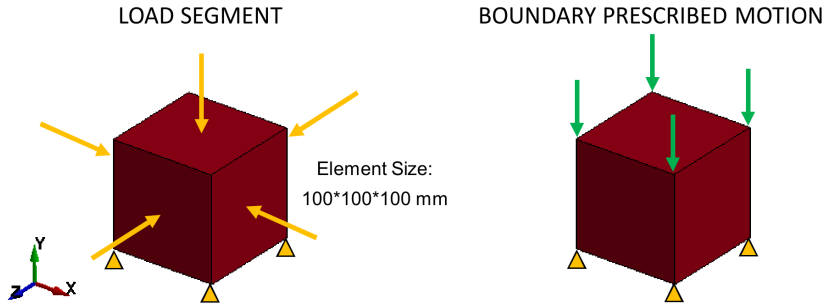

Fig.9: Single element model used to predict stress-strain response of Bank sand

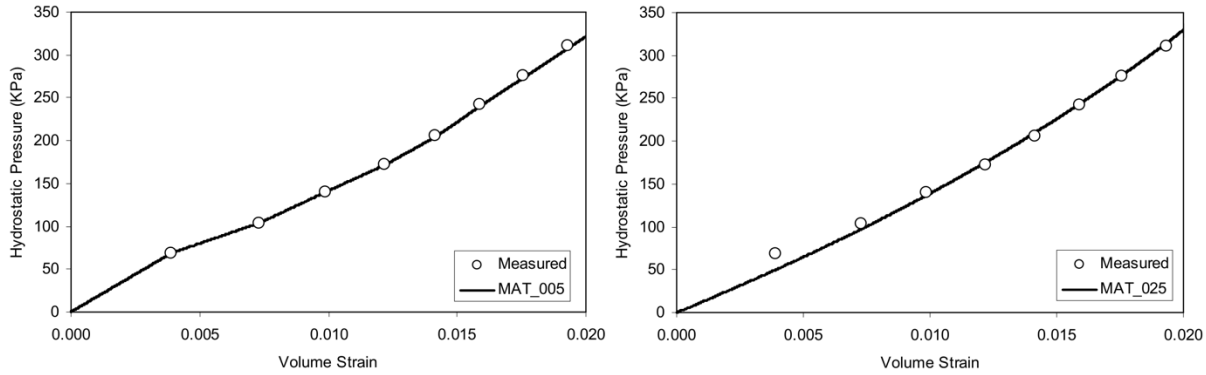

Fig.10: Comparison of experimental and numerical results for HCT (left: MAT_005, right: MAT_025)

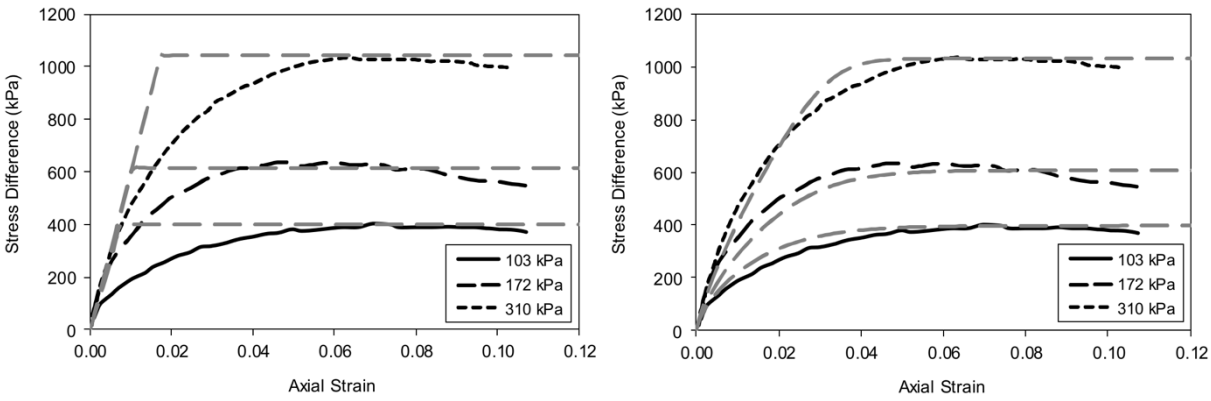

Fig.11: Comparison of experimental and numerical results for TXC (left: MAT_005, right: MAT_025)

3 Calibration of Concrete Material Models

There are several constitutive material models such as Concrete Damage Rel3, Johnson Holmquist, Continues Surface Cap Model (CSCM) and RHT in LS-DYNA material library that can predict the behavior of concrete only by defining the unconfined compressive strength. However, there is no guarantee that the predicted behavior for concrete will be sufficiently accurate. Therefore, to avoid Blind Simulation, calibration of material parameters for these model will be necessary.

In a similar manner to the previous section, first the material parameters for each model are calibrated using the TXC and HCT test data, and then the numerical results are compared with the experiments. Here the experimental data for concrete with unconfined compressive strength 48.4 MPa that is fully provided by Green and Swanson [4] has been used. The TXC and HCT test data are shown in Figure 12. The value of density and shear modulus of concrete are 24000 Kg/m^3 and 13.44 GPa, respectively [4].

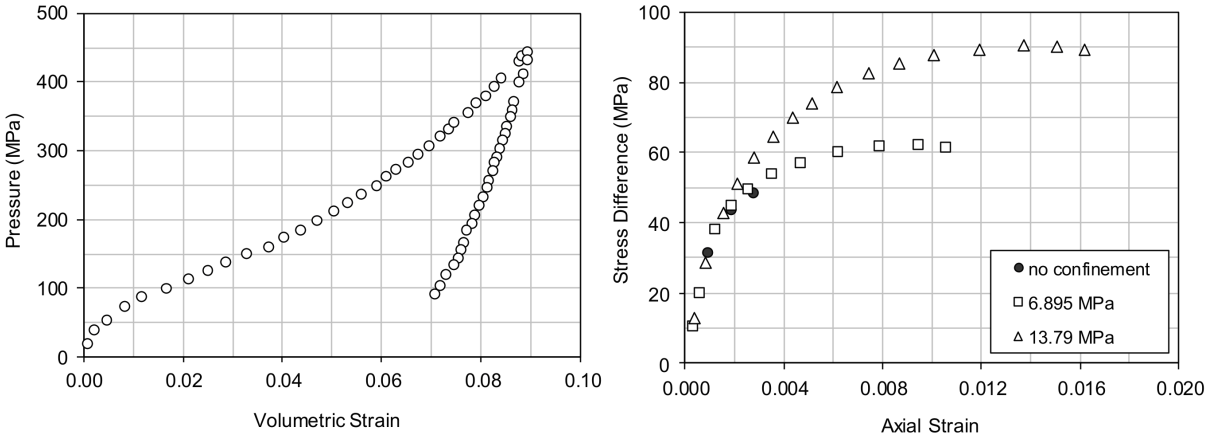

Fig.12: Experimental results for HCT (left) and TXC at different confining pressures (right) [4]

3.1 MAT_072R3 (Concrete Damage)

Mat_072R3 (Karagozian & Case (K&C) Concrete Model - Release III) is a three-invariant model that uses three independent shear failure surfaces as shown in Figure 13, which change shape depending on the level of pressure [5]. In this Figure, the curves above and below the p-axis correspond to compressive and tensile meridians, respectively. As shown in Figure 13, the response of the concrete is assumed to be linear up to the first point on the yield failure surface. After that, a hardening plasticity response happens up to the second point on the maximum failure surface. This point is the maximum strength of concrete. Afterward, softening behavior is observed up to the third point on the residual failure surface. The origin of this material model is based on the MAT_016 (Pseudo-Tensor Model) and it includes strain rate and damage effects.

In this model, three independent shear failure surfaces (initial yield, maximum and residual failure surfaces) depicted in Figure 13 are defined as follows:

$$\Delta\sigma_y = a_{0y} + \frac{p}{a_{1y} + a_{2y}p} \tag{20}$$

$$\Delta\sigma_m = a_0 + \frac{p}{a_1 + a_2 p} \tag{21}$$

$$\Delta\sigma_r = \frac{p}{a_{1f} + a_{2f}p} \tag{22}$$

Where $\Delta\sigma_y$, $\Delta\sigma_m$ and $\Delta\sigma_r$ are initial yield, maximum and residual stress respectively, a_i are input parameters determined from available laboratory data and p is hydrostatic pressure, which is positive

in compression. The maximum and residual failure surfaces can be estimated through the results of unconfined compression tests and triaxial compression tests at a range of confining pressures.
For estimate initial yield surface, Malvar et al. [6] suggest that this surface can be almost the locus of points at $\Delta\sigma = 0.45\Delta\sigma_m$ on triaxial compression paths. For the point of $(p, \Delta\sigma_m)$ located on the maximum failure surface, the corresponding point $(p', \Delta\sigma_y)$ on the initial yield surface is as explained below:

$$\Delta\sigma_y = 0.45\Delta\sigma_m \tag{23}$$

$$p' = p - \frac{0.55}{3}\Delta\sigma_m \tag{24}$$

From these equations, $\Delta\sigma_y$ and p' can be estimated from $\Delta\sigma_m$ and p, respectively. In the next one, $\Delta\sigma_y$ can be finally calculated as a function of p'. This computed curve is subsequently utilized for obtaining a regression with the following equation as the initial yield surface:

$$\Delta\sigma_y = a_{0y} + \frac{p'}{a_{1y} + a_{2y}p'} \tag{25}$$

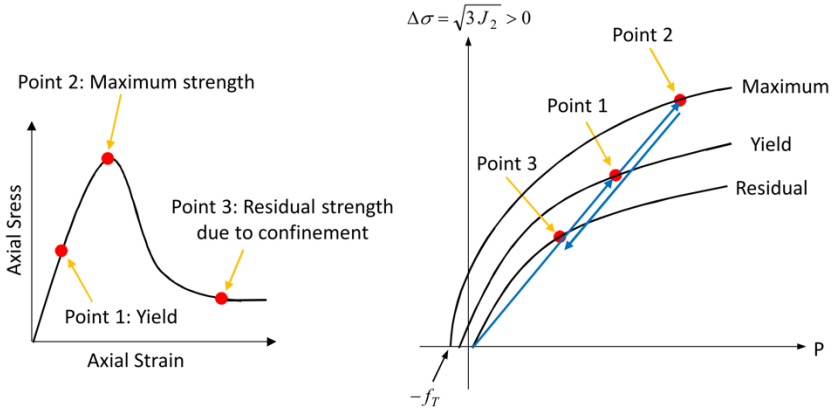

Fig.13: Schematic of the MAT_072R3 (left: illustration of the form of the stress path achievable with the three-surface form of plasticity model, right: three-surface form of plasticity model)

According to the triaxial compression test, data has shown in Figure 12 and Eqs. (23) to (25), the values of initial yield, maximum and residual failure surfaces corresponding to each confinement pressure, which are documented in Table 5.

According to calculated data presented in Table 5, the variations of $\Delta\sigma_m$ versus p are shown in Figure 14. According to Eq. (21), a_0, a_1 and a_2 are estimated as 27, 0.81, -0.0025, respectively. Similarly, the other coefficients for the yield and residual failure surface are estimated. Parameters calibrated for MAT_72R3 are summarized in Table 6. Other parameters related to the tensile or extension meridian and damage accumulation are generated by the automatic option of MAT_72R3.

p (MPa)	p' (MPa)	$\Delta\sigma_y$ (MPa)	$\Delta\sigma_m$ (MPa)	$\Delta\sigma_r$ (MPa)
16.13	7.26	21.78	48.40	48.40
27.73	16.27	28.13	62.50	61.00
43.79	27.29	40.50	90.00	89.00

Table 5: Estimation of failure surfaces versus p for MAT_072R3

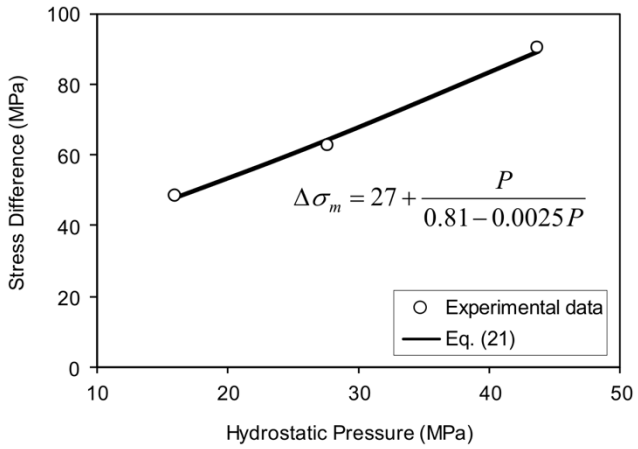

Fig.14: Maximum failure surface fitting by MAT_072R3

Yield surface		Maximum surface		Residual surface	
a_{0y} (MPa)	15	a_0 (MPa)	27	a_{1f}	0.3
a_{1y}	1.14	a_1	0.81	a_{2f} (MPa^{-1})	0.005
a_{2y} (MPa^{-1})	-0.0025	a_2 (MPa^{-1})	-0.0025		

Table 6: Material parameters calibrated through experimental data for MAT_072R3

In this material model similar to the MAT_005 (Soil and Foam), the hydrostatic pressure is defined based on the volumetric strain using Eq. (8). The calculated values are expressed in tabular form (up to 10 point) using the Tabulated Compaction equation of state. According to a hydrostatic compression test, data has shown in Figure 12 and Eq. (8), the volumetric strain corresponding to each hydrostatic pressure, which is documented in Table 7.

ε_{kk}	$\ln(V/V_0)$	p (MPa)
0.0025	-0.0025	36
0.005	-0.0050	50
0.020	-0.0202	110
0.040	-0.0408	170
0.060	-0.0619	250
0.080	-0.0834	370
0.090	-0.0943	450

Table 7: Hydrostatic pressure as a function of volumetric strain

3.2 MAT_111 (Johnson Holmquist Concrete)

This model can be used for concrete subjected to large strains, high strain rates and high pressures, and was developed by Holmquist et al. [7]. The equivalent strength is expressed as a function of the pressure, strain rate, and damage. The pressure is expressed as a function of the volumetric strain and includes the effect of permanent crushing. The damage is accumulated as a function of the plastic volumetric strain, equivalent plastic strain and pressure. In this model, the equivalent stress is defined as Eq. (26).

$$\sigma_{eq} = f_c' \left[A(1-D) + B\left(\frac{p}{f_c'}\right)^N \right] \left[1 - C\ln\left(\frac{\dot{\varepsilon}}{\dot{\varepsilon}_0}\right) \right] \tag{26}$$

Where f_c' is the uniaxial compressive strength, D is the damage parameter, p is hydrostatic pressure, A, B and N are constant parameters which can be estimated through the results of unconfined compression tests and triaxial compression tests at a range of confining pressures, C is strain rate parameter, $\dot{\varepsilon}_0$ is reference strain rate and $\dot{\varepsilon}$ is current strain rate.

In this mode, damage parameter D incrementally accumulates both from equivalent plastic strain $\Delta\varepsilon_p$ and plastic volumetric strain $\Delta\mu_p$, and is expressed as

$$D = \sum \frac{\Delta\varepsilon_p + \Delta\mu_p}{D_1\left(P^* + T^*\right)^{D_2}} \tag{27}$$

Where D_1 and D_2 are material constants, $p^* = p/f_c'$ is the normalized pressure and $T^* = T/f_c'$ is the normalized maximum tensile hydrostatic pressure.

The plot of hydrostatic pressure-volumetric strain in a hydrostatic compression test can be separated into three different response regions as shown in Figure 15:

1. The first region is linear elastic and occurs at $P \le P_{crush}$. P_{crush}, and μ_{crush} are the pressure and volumetric strain respectively that occur in a uniaxial stress compression.

2. The second region is referred to as the transition region and occurs at $P_{crush} < P < P_{lock}$. In this region, the air voids are gradually compressed out of the concrete producing plastic volumetric strain. Unloading in this region occurs along a modified path that is interpolated from the adjacent regions.

3. The third region defines the relationship for fully dense material (all air voids removed from the concrete). The air voids are completely removed from the material when the pressure reaches P_{lock} with the corresponding μ_{lock} (both user inputs) and the relationship is expressed as:

$$p = K_1\overline{\mu} + K_2\overline{\mu}^2 + K_3\overline{\mu}^3 \tag{28}$$

Hitherto K_1, K_2, and K_3 are material constants and $\overline{\mu}$ denotes the modified volumetric which is expressed by the following equation in terms of the locking volumetric strain μ_{lock}:

$$\overline{\mu} = \frac{\mu - \mu_{lock}}{1 + \mu_{lock}} \tag{29}$$

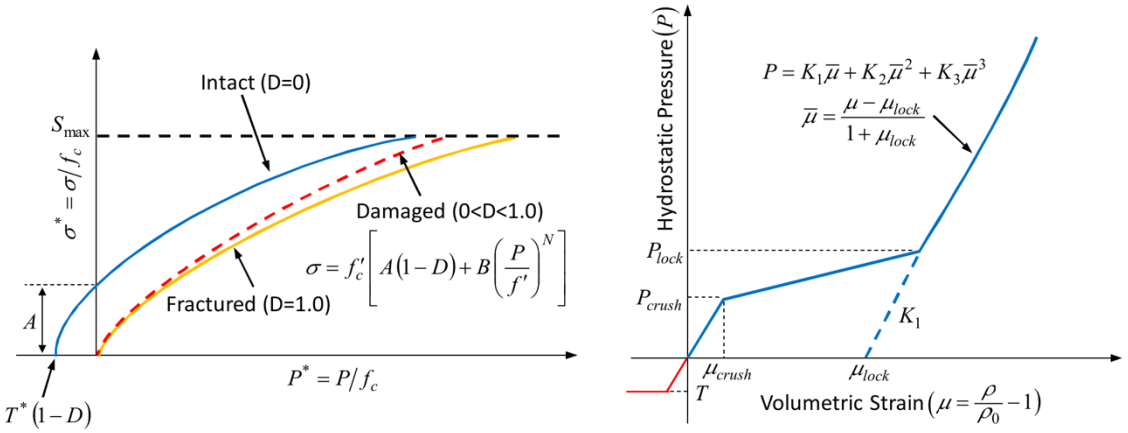

Fig.15: Schematic of the MAT_111 (left: The shear-pressure strength response, right: pressure–volume response)

For the intact material ($D = 0$) in the reference strain rate ($\dot{\varepsilon} = \dot{\varepsilon}_0$), the Eq. (26) can be written as

$$\sigma_{eq} = f_c'\left[A + B\left(\frac{p}{f_c'}\right)^N\right] \tag{30}$$

According to triaxial compression test data has shown in Figure 12, the variations of σ_{eq} versus p are shown in Figure 16. According to Eq. (30), A, B and N are estimated as 0.0, 2.27, 0.761, respectively.

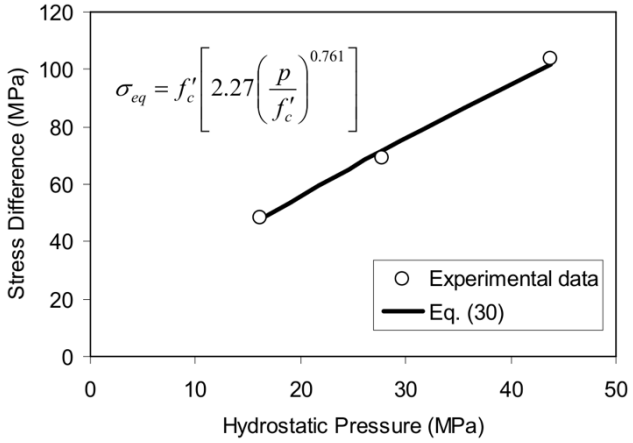

Fig.16: The shear-pressure strength response fitting by MAT_111

Parameters calibrated for MAT_111 are summarized in Table 8. The Poisson's ratio ν of concrete-like materials is generally taken to be 0.2. The elastic modulus E and maximum tensile hydrostatic pressure T can be simply determined using the following equations proposed by ACI [8].

$$E = 0.043 \rho_0^{3/2} \sqrt{f_c} \tag{31}$$

$$T = 0.62 \sqrt{f_c} \tag{32}$$

Some of the parameters involved in the pressure–volume law can easily be identified. For instance, from elasticity P_{crush} and μ_{crush} can be obtained using the following equations [9].

$$P_{crush} = f_c / 3 \tag{33}$$

$$\mu_{crush} = f_c (1 - 2\nu) / E \tag{34}$$

Other parameters related to the equation of state and damage parameter are taken from the values recommended by Ren et al. [10].

Strength		Pressure-Volume		Damage	
A	0.0	P_{crush} (MPa)	16.13	D_1	0.04
B	2.27	μ_{crush}	0.001	D_2	0.04
N	0.761	P_{lock} (MPa)	3470		
f_c' (MPa)	48.4	μ_{lock}	0.1		
T	4.31	K_1 (GPa)	116		
$S_{\max}$	7.0	K_2 (GPa)	-243		
		K_3 (GPa)	506		

Table 8: Material parameters calibrated through experiment data for MAT_111

3.3 MAT_159 (Continuous Surface Cap Model)

This model is a continuous surface cap model with a smooth intersection between the shear surface and the hardening cap. It was developed in 1990s for roadside safety analysis and was made available in LS-DYNA around 2005 [11]. In this model, the initial damage surface coincides with the yield surface and the strain rate effects are modeled with visco-plasticity.

The Continuous Surface Cap Model (CSCM) combines the shear (failure) surface with the hardening compaction surface (cap) by using a multiplicative formulation. The yield function is defined in terms of three stress invariants as Eq. (35).

$$Y(I_1, J_2, J_3) = J_2 - \Re(J_3)^2 F_f^2(I_1) F_c(I_1, \kappa) \tag{35}$$

Where $F_f(I_1)$ is the shear failure surface, $F_c(I_1, k)$ is the hardening cap with κ to be the cap hardening parameter and $\Re(J_3)$ is the Rubin three-invariant reduction factor [12]. The multiplicative form allows the cap and shear surface to be combined continuously and smoothly at their interaction. Similar to MAT_025, the shear failure surface $F_f(I_1)$ is defined as Eq. (36).

$$F_f(I_1) = \alpha - \lambda \exp(-\beta I_1) + \theta I_1 \tag{36}$$

Where I_1 is first stress invariant and several constants α, θ, λ and β are material constant that are determined from triaxial compression test data.

In this material model, the hydrostatic pressure is defined based on the plastic volume strain as Eq. (37).

$$\varepsilon_v^p = W\left[1 - e^{-D_1(X - X_1) - D_2(X - X_1)^2}\right] \tag{37}$$

Where ε_v^p is the plastic portion of the volume strain, W characterizes the maximum plastic volumetric strain as shown in Figure 7, D_1 and D_2 are constant parameters which determine the shape of the pressure-volume strain curve, X represents the first invariants of the stress tensor and X_1 is pressure at which compaction initiates in isotropic compression, i.e. $X - X_1 = 3(P - P_1)$.

According to triaxial compression test data shown in Figure 12, the values of $\sqrt{J_2}$ are calculated in terms of I_1 for different values of confinement pressure σ_3, which are documented in Table 9. Note that in the triaxial compression test $p = \sigma_1 + 2\sigma_3$. As shown in Figure 17, a function was fitted to the plot of $\sqrt{J_2}$ versus I_1. According to the regression analysis and Eq. (36), the constant material parameters of α, θ, λ and β are obtained as 13.073, 0.292, 0.0, and 0.0, respectively.

σ_3 (MPa)	$\sigma_1 - \sigma_3$ (MPa)	p (MPa)	I_1 (MPa)	$\sqrt{J_2}$
0.00	48.40	16.13	48.40	780.85
6.90	62.50	27.73	83.19	1302.08
13.79	90.00	43.79	131.37	2700.00

Table 9: Estimation of I_1 versus $\sqrt{J_2}$ for MAT_159

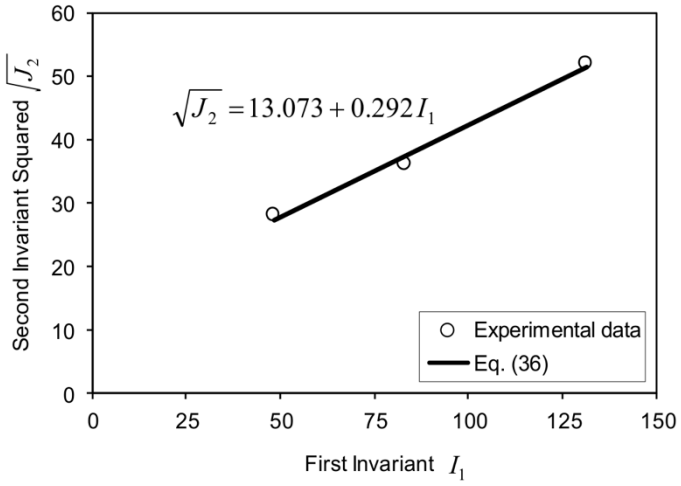

Fig.17: Variations of $\sqrt{J_2}$ versus I_1 fitting by MAT_159

To estimate D_1 and D_2, a trial and error procedure was used utilizing an initial value for W to have the best curve fitting. According to hydrostatic compression test data shown in Figure 12, the values of $-\ln\left(1-\varepsilon_v^p/W\right)$ are calculated in terms of $X - X_1$ by assuming $W = 0.07$, which are documented in Table 10. As shown in Figure 18 and Eq. (37), the parameters of D_1 and D_2 are estimated as 0.0013 and 2E-7, respectively. Material parameters calibrated for MAT_159 are summarized in Table 3. Other parameters were taken from typical values reported by Murray in her material user's manual for the FHWA [13].

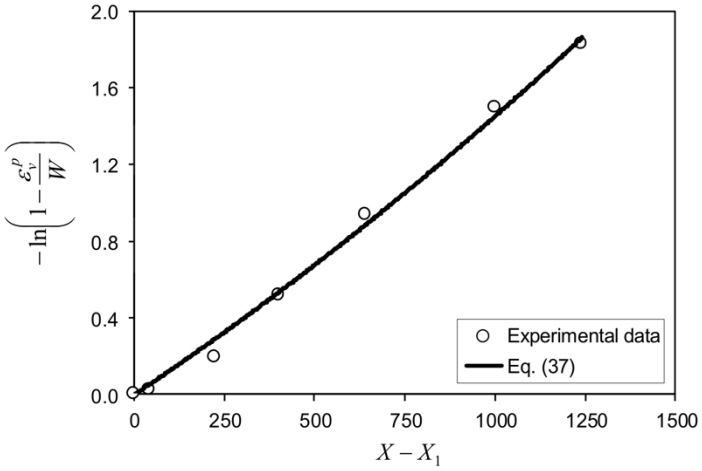

Fig.18: Estimation of the relationship between hydrostatic pressure and plastic volume strain by MAT_159

Yield surface		Plastic volume strain	
α (MPa)	13.073	R	0.6
θ (MPa)	0.292	X_0 (MPa)	108
λ (MPa)	0.0	W	0.07
β (MPa)	0.0	D_1 (MPa^{-1})	0.0013
		D_2 (MPa^{-2})	2.0E-7

Table 10: Material parameters calibrated through experiment data for MAT_159

3.4 Numerical validation of constitutive material models

The numerical model was conducted with the same size of the test specimens. The diameter and length of the cylinder specimens were 68.6mm (2.7 in.) and 52.4mm (6.0 in.), respectively. The numerical model is shown in Figure 19. Similar to previous section, before each triaxial test, the cylinder is

subjected to isotropic load until it reaches the desired confining pressure using the keyword “LOAD SEGMENT”. Subsequently, for each confining pressure, the cylinder is loaded axially in compression using the keyword “BOUNDARY PRESCRIBED MOTION”. Also, only the movement of the nodes of the bottom surface of the cylinder is limited in the vertical direction. Axial stress was calculated as difference between the (axial force/original cross sectional area) and confinement, while the axial strain was calculated as difference between the (top axial displacement/initial height) and strain due to confinement.

Comparisons of the numerical results with TXC test data reported by Green and Swanson [4] for different constitutive material models are shown in Figures 20. As can be seen, all calibrated material models were able to predict the TXC test well. Nevertheless, MAT_025 and MAT_072R3 were able to predict TXC significantly better than MAT_111 and MAT_159. Of course, calibration MAT_159 damage parameter seems to be effective in improving its accuracy.

Moreover, numerical results show that to avoid Blind Simulation, the calibration of material parameters for these models are necessary (see Figure 21).

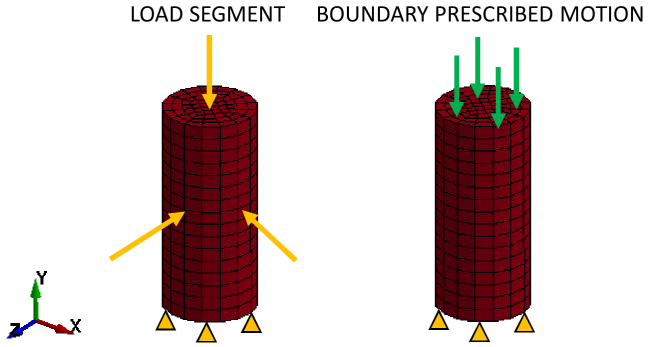

Fig.19: Cylinderical model used to predict stress-strain response of concrete

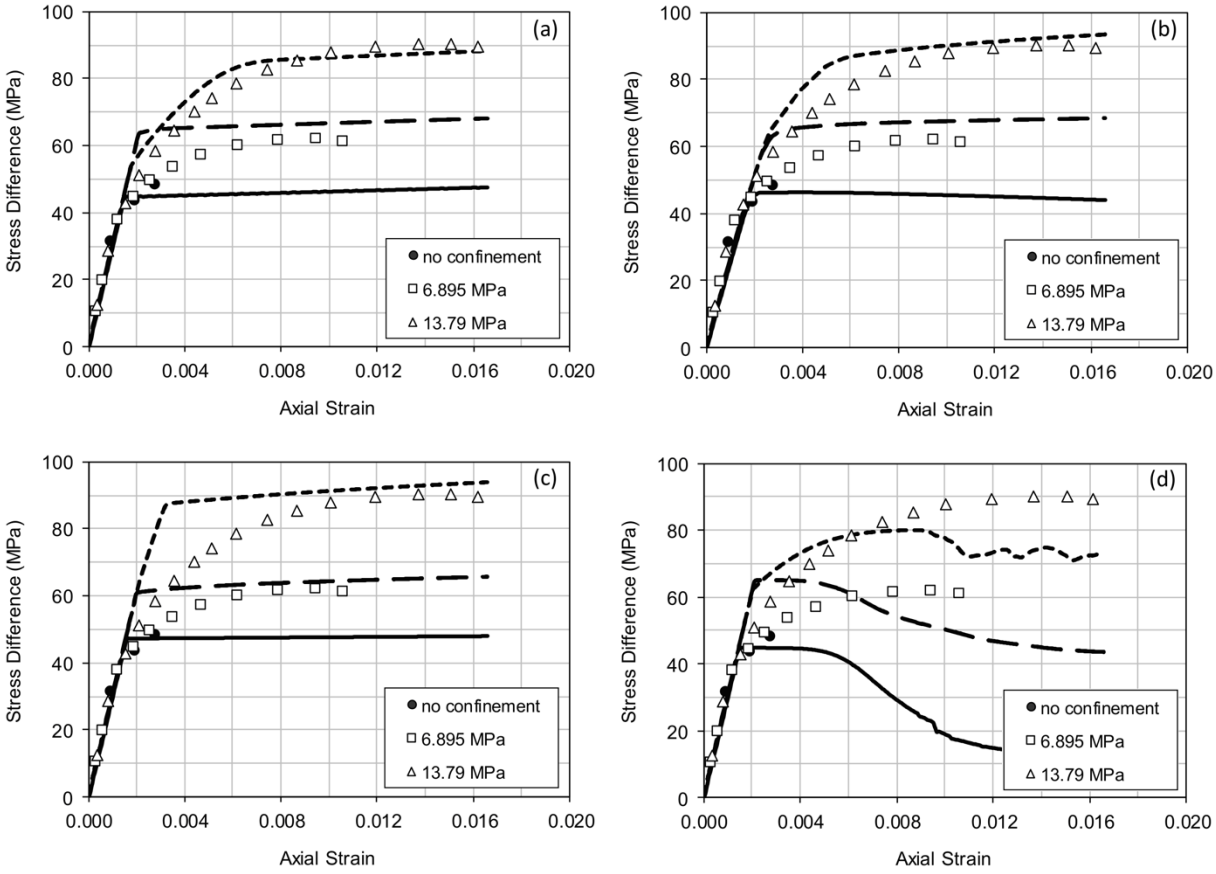

Fig.20: Comparison of experimental and numerical results for TXC (a: MAT_025, b: MAT_072R3, c: MAT_111, d: MAT_159)

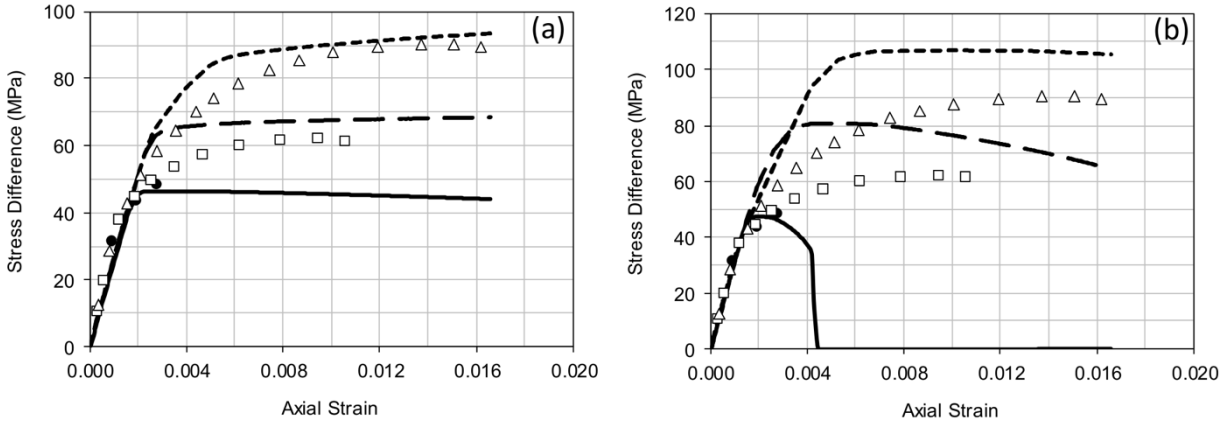

Fig.21: Comparison of experimental and numerical results for TXC (a: MAT_072R3 (calibrated), b: MAT_072R3 (input generation))

4 Summary

In this paper, six constitutive material models, MAT_005 (Soil and Foam), MAT_025 (Geologic Cap Model), MAT_072R3 (Concrete Damage Model), MAT_111 (Johnson and Holmquist Concrete) and MAT_159 (Continuous Surface Cap Model) in LS-DYNA material library were calibrated for geomaterial using TXC (triaxial Compression Test) and HCT (hydrostatic compression tests) test data.

First, the calibration process for the determination of the material parameters for each model was discussed in detail. Then, the accuracy of each model was evaluated in predicting stress-strain behaviors of the geomaterial in compression under different confining pressures.
Moreover, our results showed that, although the constitutive material models such as Concrete Damage Rel3, Johnson Holmquist, Continues Surface Cap Model (CSCM) can predict the behavior of concrete only by defining the unconfined compressive strength, but to avoid Blind Simulation, calibration of material parameters for these models are necessary.

Our future work will be to calibrate the damage parameter of these models in order to improve their accuracy.

5 Literature

[1] Z. Z. Lee, N. Y. Chang, K. T. Chang et al., Determination of cap model parameters using drained convectional triaxial compression test results, Proc. 27th Annual USSD Conference, 2007.

[2] M. M. Zaman, C. S. Desai, M. O. Faruque, ,An Algorithm for determining parameters for cap model from raw laboratory test data, Proc. 4th Int. Conf. Numer. Methods Geomech., 1982

[3] S. Sture, C. S. Desai, C. S., R. Janardhanam, Development of a Constitutive Law for an Artificial Soil, Proc. 3rd Int. Conf. Numer. Methods Geomech., 1979.

[4] S. J. Green, S. R. Swanson, Static constitutive relations for concrete. Air Force Weapons Laboratory (Technique Report No. AFWL-TR-72-2), Kirtland Air Force Bace, 1973

[5] J. E. Crawford, J. M. Magallanse, S. Lan, Y. Wu, User's manual and documentation for release III of the K&C concrete material model in LS-DYNA, TR-11-36-1, Technical Report, Karagozian & Case, 2011

[6] J. Malvar, J. Crawford, J. Wesevich, D. Simons, A plasticity concrete material model for Dyna3D, International Journal of Impact Engineering, 19 (1997) 847-873.

[7] T. J. Holmquist, G. R. Johnson, W. H. Cook, A computational constitutive model for concrete subjected to large strains, high strain rates, and high pressures. In: The 14th international symposium on ballistic, 1993

[8] American Concrete Institute (ACI) ACI Committee 318: Building Code Requirements for Reinforced Concrete (ACI 318-89) and Commentary (318R-89). Farmington Hills, MI: ACI (1989)

[9] M. P. Loria, O.S. Hopperstad, T. Børvik, T. Berstad, Numerical predictions of ballistic limits for concrete slabs using a modified version of the HJC concrete mode, International Journal of Impact Engineering 35 (2008) 290 – 303.

[10] G. M. Ren, H. Wu, Q. Fang, X. Z. Kong, Parameters of Holmquist–Johnson–Cook model for high strength concrete like materials under projectile impact, International Journal of Protective Structures, (2017) 1- 16.
[11] Y. D. Murray, A. Abu-Odeh, R. Bligh, Evaluation of concrete material model 159, FHWA-HRT-05-063, 2006.
[12] M. Rubin, A simple isotropic failure surface, ASCE journal engineering mechanics, 117 (1991) 348-369.
[13] Y. D. Murray, User‘s manual for LS-DYNA concrete material model 159, FHWA-HRT-05-062, 2007.